

## Colliding-Droplet Microreactor: Rapid On-Demand Inertial Mixing and Metal-Catalyzed Aqueous Phase Oxidation Processes

Ryan D. Davis,<sup>1</sup> Michael I. Jacobs,<sup>1, 2</sup> Frances A. Houle,<sup>1</sup> and Kevin R. Wilson<sup>1</sup>

<sup>1</sup>Chemical Sciences Division, Lawrence Berkeley National Laboratory, Berkeley, California 94720, United States

<sup>2</sup>Department of Chemistry, University of California, Berkeley, California 94720, United States.

### **Table of Contents**

Page S-2.	<i>Figure S1.</i> Bulk rhodamine fluorescence emission with added acid. <i>Figure S2.</i> Excitation LED spectrum.
Page S-3.	<i>Figure S3.</i> Colliding RhB with pure water droplets: demonstrating the change in droplet velocity after collision and the behavior of $I_x$ in the absence of acid. <i>Figure S4.</i> Rhodamine B calibration curve.
Page S-4.	<i>Figure S5.</i> $\Delta x$ and MSE for mixing at low velocity ( $U = 0.21 \pm 0.02$ m/s).
Page S-5	<i>Figure S6.</i> Brightfield mages and illustrated representations of internal flows for microdroplet collisions at high velocity. <i>Figure S7.</i> Droplet separation/fragmentation without mixing completely.
Page S-6	<i>Figure S8.</i> Brightfield images of collisions at low velocity ( $U = 0.5$ m/s). <i>Figure S9.</i> Experimentally-determined $\tau$ as a function of $We$ number.
Page S-7	<i>Figure S10.</i> Timescales for 10 $\mu\text{m}$ colliding microdroplets. <i>Figure S11.</i> Experiment vs. simulation with Fenton reaction rate = $50 \text{ M}^{-1}\text{s}^{-1}$ .
Page S-8.	Table S1. Reaction rate coefficients used in the simulations. Expanded experimental detail of brightfield image analysis.
Page S-9	<i>Additional discussion begins:</i> Estimated Linear Oscillation Frequency Microdroplet Coalescence vs. Separation.
Page S-10	Additional Discussion of Relating $\tau$ to Microdroplet Fluid Dynamics Generalizations of Mixing Dynamics.
Page S-11	Sample Volume Consumption Rates.

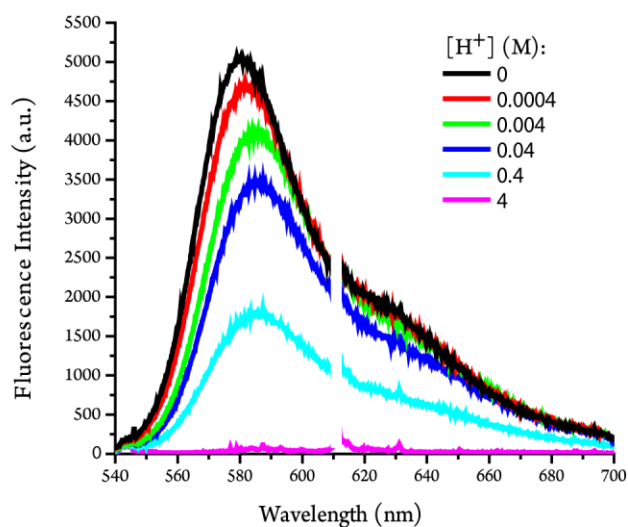


**Figure S1.** Change in RhB fluorescence intensity as a function of added acid concentration from 0 to 4 M (at added  $[H^+]$  of 0, pH = 7).

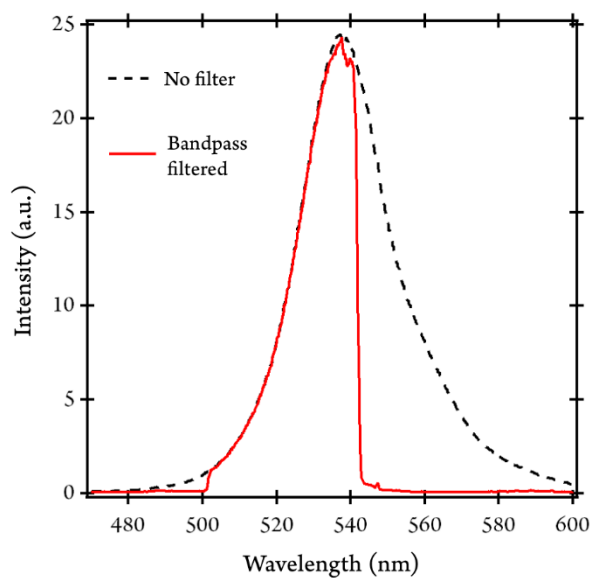


**Figure S2.** Spectrum of the excitation LED with and without the bandpass filter. Experiments were performed with the bandpass filter in place.

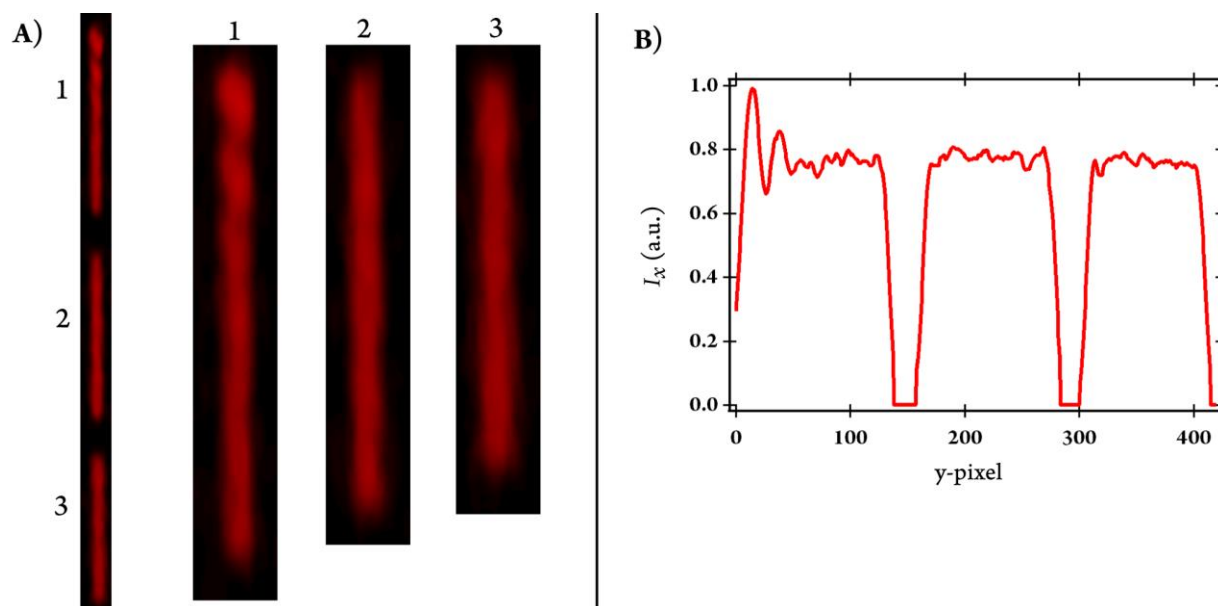


**Figure S3.** Colliding RhB droplets with distilled water droplets ( $U = 2.1 \pm 0.2$  m/s) to demonstrate (A) an example of the change in velocity as droplets fell post-collision for a stream of RhB<sub>(aq)</sub> microdroplets colliding with a stream of distilled water microdroplets, with the full scale image snapshot (left) and cropped images of each pulse (right); and (B)  $I_x$  as a function of y-pixel, demonstrating that  $I_x$  does not decrease appreciably in the absence of acid, with a small decrease (to  $\sim 80\%$  of the initial value) attributable to dilution and relaxation of shape oscillations.

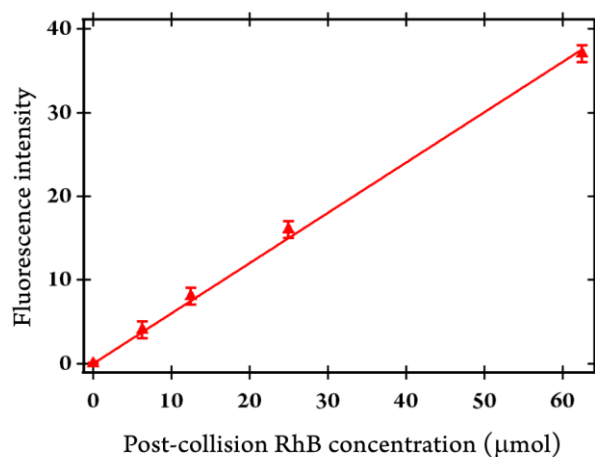


**Figure S4.** Post-collision fluorescence intensity as a function of RhB concentration. Data points were obtained by colliding RhB<sub>(aq)</sub> droplets with FeCl<sub>2(aq)</sub> droplets and measuring the post-collision fluorescence intensity. The slope of the best fit line is  $0.60 \pm 0.05$  and the intercept is  $0.0 \pm 0.3$  (95% confidence interval).

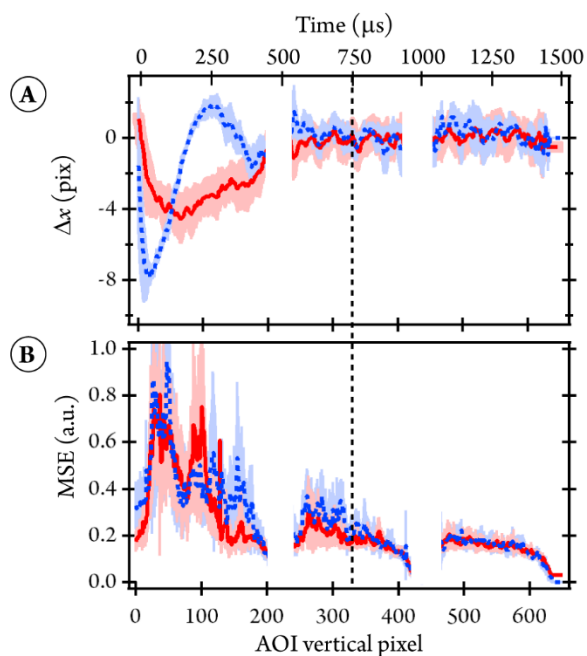


**Figure S5.** Mixing of 125  $\mu\text{M}$   $\text{RhB}_{(\text{aq})}$  microdroplets with 20%  $\text{H}_2\text{SO}_4$  microdroplets at low velocity ( $U = 0.21 \pm 0.02$  m/s) for different impact parameters ( $X = 0.0 \pm 0.1$  and  $0.8 \pm 0.1$ ). **(A)** Plot of  $\Delta x$  vs.  $y$  (time) for the experiment shown in Fig. 4 of the main text. **(B)** Plot of MSE vs.  $y$  (time) for the experiment shown in Fig. 4 of the main text. The shaded areas represent  $\pm 1$  SD of twenty collected images. The dashed line indicates the approximate value of  $\tau$  ( $750 \pm 50$  and  $760 \pm 50$   $\mu\text{s}$  for  $X = 0$  and  $0.8$ , respectively)

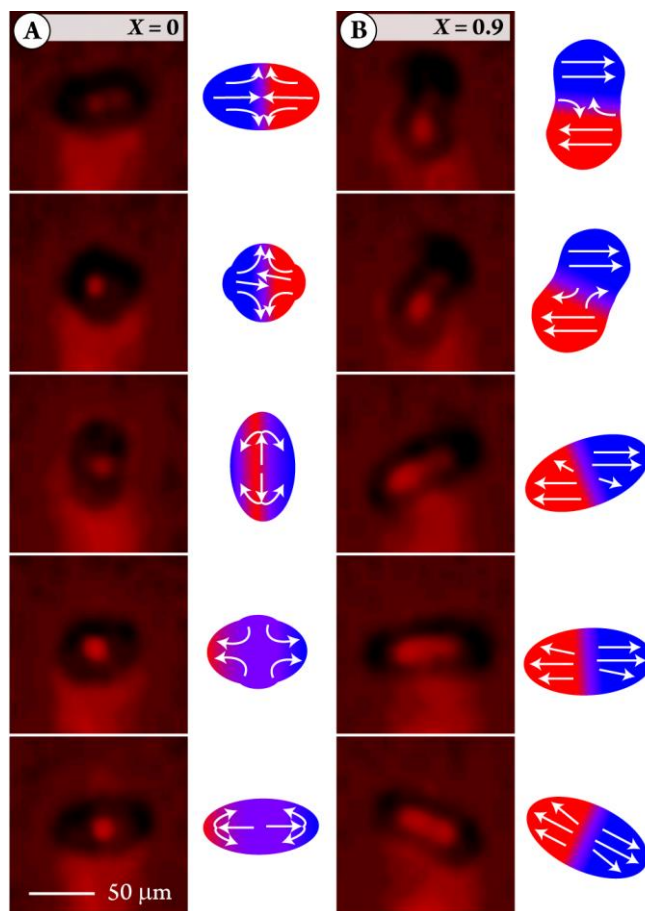


**Figure S6.** Brightfield images and illustrated representations of internal flows for microdroplet collisions at high velocity ( $U = 3.9 \pm 0.2$  m/s) for  $X = 0$  (A) and 0.9 (B). Time difference between images is  $\sim 5 \mu\text{s}$  ( $\Delta t_{\text{BF}} \approx 0$  to 20  $\mu\text{s}$ ). Illustrations are representations of simulations from refs. 23 and 24.

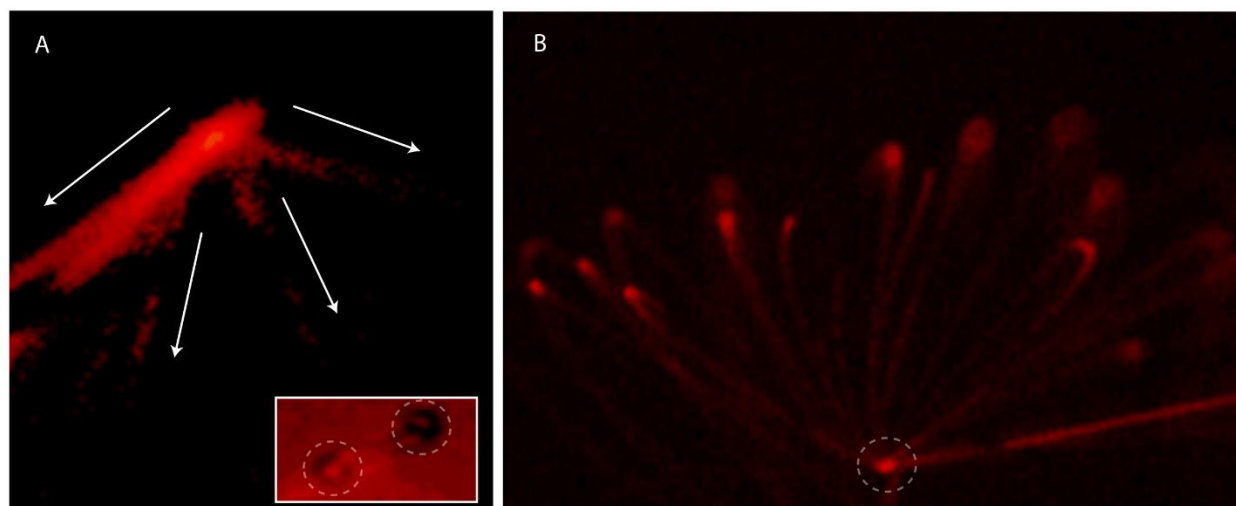


**Figure S7.** (A) Separating droplet collision at  $U = 7.4 \pm 0.1$  m/s and  $X \approx 0.9 \pm 0.1$ . The white arrows indicate the observable droplets. In addition to the main droplets, several satellite droplet trails are apparent. It is evident that partial but incomplete mixing occurred by the weak fluorescence emission in the droplet trajectory of the  $\text{H}_2\text{SO}_{4(\text{aq})}$  droplet (which was moving left to right). The inset shows a brightfield snapshot during the stretching and separation process. The main droplets are indicated by the dashed circle. (B) A droplet collision that resulted in fragmentation at  $U = 7.4 \pm 0.1$  m/s. The point of collision is indicated by the dashed circle.

Multiple droplet fragments formed, as evident by the number of streaks moving away from the point of collision.

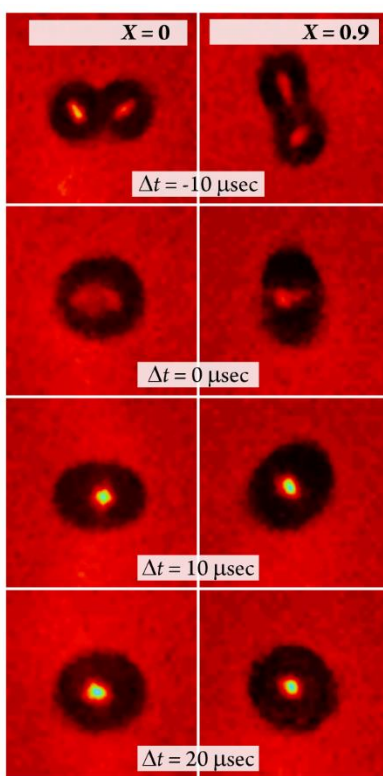


**Figure S8.** Brightfield images of collisions at low velocity ( $U = 0.5$  m/s).

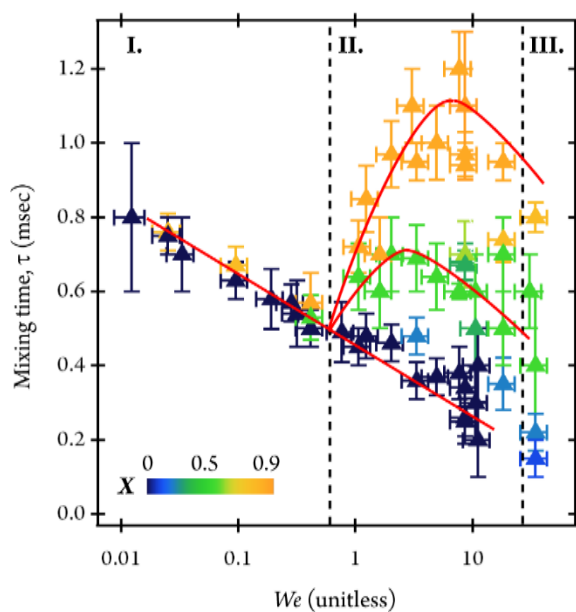


**Figure S9.** Experimentally-determined  $\tau$  as a function of  $We$  (Eq. S2). Uncertainty in  $We$  is propagated ( $1\sigma$  level) from  $D$  and  $U$  in Eq. S2. Solid red lines indicate trends in  $\tau$  for  $X \approx 0, 0.5$ , and  $0.9$ . Vertical dashed lines indicate regions where different mixing behavior is observed.

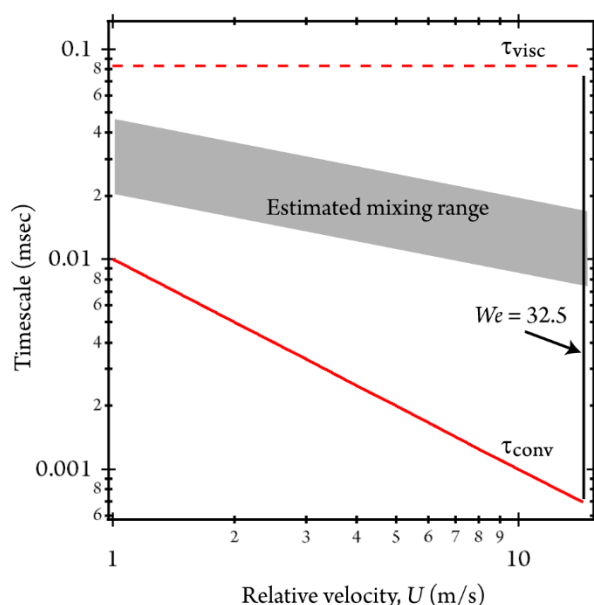


**Figure S10.** Predicting  $\tau$  from  $\tau_{\text{conv}}$  and  $\tau_{\text{visc}}$  for 10  $\mu\text{m}$  diameter colliding microdroplets. In the experiments reported in the main text,  $\tau$  remained between  $\tau_{\text{conv}}$  and  $\tau_{\text{visc}}$  for the 40  $\mu\text{m}$  diameter microdroplets. Assuming this holds true for 10  $\mu\text{m}$  droplets, mixing times of  $\sim 10$  to  $20 \mu\text{s}$  are possible at the highest velocity ( $\sim 14 \text{ m/s}$ ) that is below the predicted separation threshold for 10  $\mu\text{m}$  colliding microdroplets ( $We = 32.5$ , slightly higher than the threshold for the 40  $\mu\text{m}$  microdroplets)<sup>24</sup>, i.e., above  $\sim 14$  to  $15 \text{ m/s}$ , 10  $\mu\text{m}$  colliding microdroplets are predicted to separate or fragment, depending on collision geometry.

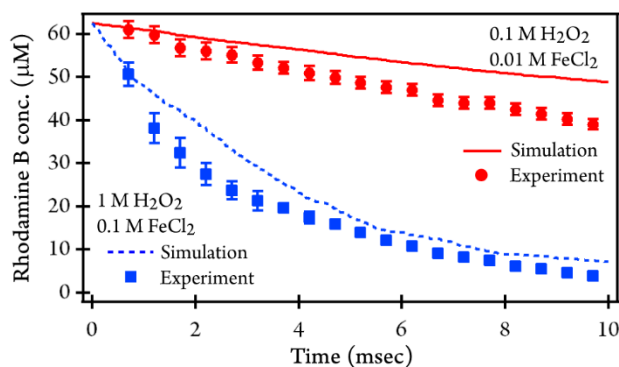


**Figure S11.** Experimental Fenton chemistry results compared to simulation with a rate constant of  $50 \text{ M}^{-1}\text{s}^{-1}$  for the initial Fenton reaction ( $\text{Fe}^{2+} + \text{H}_2\text{O}_2$ ).

**Table S1. Reactions and rate constants for kinetic simulations.**

Reaction	Rate ( $\text{M}^{-1}\text{s}^{-1}$ )	Ref.
$\text{Fe}^{2+} + \text{H}_2\text{O}_2 \rightarrow \text{Fe}^{3+} + \text{OH}^- + \cdot\text{OH}$	76 *	16
$\cdot\text{OH} + \text{RhB} \rightarrow \text{RhBOH (products)}$	$3.4 \times 10^{9\dagger}$	30
$\cdot\text{OH} + \text{Fe}^{2+} \rightarrow \text{Fe}^{3+} + \text{OH}^-$	$3.2 \times 10^8$	16
$\cdot\text{OH} + \text{H}_2\text{O}_2 \rightarrow \text{HO}_2\cdot + \text{H}_2\text{O}$	$3.3 \times 10^7$	16
$\cdot\text{OH} + \cdot\text{OH} \rightarrow \text{H}_2\text{O}_2$	$6 \times 10^9$	16
$\cdot\text{OH} + \text{RhBOH} \rightarrow \text{secondary products}$	$3.4 \times 10^{9\dagger}$	30

\*A range of values is reported in the literature from 50 to  $76 \text{ M}^{-1}\text{s}^{-1}$ .<sup>12,16</sup> Simulations were also run with the lower value of  $50 \text{ M}^{-1}\text{s}^{-1}$ , as shown in Figure S11.

<sup>‡</sup>Reaction rate coefficient reported for rhodamine 6G, which is structurally similar to RhB.

<sup>†</sup>The reaction rate coefficient for this reaction is not reported. Thus, we approximate it here using the value for the primary reaction<sup>32</sup>.

## Expanded Experimental Detail

**Brightfield Image Analysis.** As shown in Figure 3B of the main text for the red-plane image extraction, the short ( $\leq 1 \mu\text{s}$ ) brightfield LED pulses provide snapshots of the physical characteristics of droplets (post- and pre-merged) at a specific point in time. During an experiment, brightfield images are used to guide collisions and set time zero for the collision ( $t_0$ ). The timing of the brightfield LED pulse relative to  $t_0$  ( $\Delta t_{BF}$ ) is then phase shifted by  $-10$  to  $-100 \mu\text{s}$ , which does not influence the droplet trajectories or  $t_0$ , but allows the droplet stream to be imaged prior to (or after) the collision, which is necessary to determine the droplet diameters  $D_1$  and  $D_2$ , droplet velocities  $v_1$  and  $v_2$ ,  $\alpha$ , and the separation distance  $b$  between the centers of the colliding droplets.<sup>17,18</sup> Phase shifting the brightfield LED pulse is not necessary at low velocities when trailing droplets in the droplet stream are imaged simultaneously. In these cases,  $v_1$  and  $v_2$  are determined from the known time spacing between sequential droplets (i.e.,  $500 \mu\text{s}$  for a droplet generation rate of  $2 \text{ kHz}$ ).

Brightfield images cannot be completely isolated from the yellow RhB fluorescence emission, which registers intensity on both the red and green pixel planes. However, this does not impact the determination of the collision parameters from brightfield images. Once the collision parameters are set, the brightfield LED is turned off to minimize background noise in the fluorescence emission images.



## Additional Discussion

**Estimated Linear Oscillation Frequency.** The angular oscillation frequency ( $\omega$ ) of a coalesced droplet is given by Eq. S1

$$\omega^2 = \frac{l(l-1)(l+2)\sigma}{R^3\rho} \quad (\text{S1})$$

where  $l$  is the mode order corresponding to a characteristic droplet shape oscillation,  $R$  is droplet radius,  $\rho$  is fluid density, and  $\sigma$  is the fluid surface tension.<sup>25</sup> The linear oscillation frequency is given by  $\omega/2\pi$ .<sup>25</sup> Droplet shape oscillations will appear as oscillations in  $I_x$  at a frequency consistent with the linear oscillation frequency, similar to observations of Bzdek et al.<sup>25</sup> with elastically scattered laser light.

For mode order  $l = 2$ , a radius of 20  $\mu\text{m}$ , and using  $\rho$  and  $\sigma$  values of 1160  $\text{kg m}^{-3}$  and 73.9  $\text{mN m}^{-1}$ , respectively (values associated with 20%  $\text{H}_2\text{SO}_{4(\text{aq})}$ ),  $\omega/2\pi \approx 40$  kHz (25  $\mu\text{s}$  period). This linear oscillation frequency of 40 kHz and period of 25  $\mu\text{s}$  is consistent with the oscillations observed in  $I_x$  in Fig. 5B (for  $X = 0$ ) of the main text, indicating these oscillations in  $I_x$  are a result of droplet shape deformations associated with coalescence.

**Microdroplet Coalescence vs. Separation.** Depending on the initial energy of a collision, microdroplet collisions can have different observable outcomes. These outcomes can be categorized as bouncing, partial coalescence, permanent coalescence, separation, or shattering.<sup>17,18,23,24</sup> Bouncing and partial coalescence were not observed in the experiments reported in the main text. At all relative velocities below  $\sim 7$  m/s, permanent coalescence was the observed outcome. Above  $\sim 7$  m/s, permanent coalescence was the most common outcome for  $X = 0.2$  to 0.8, but above  $X = 0.9$ , separation was observed, as seen in Figure S7A. Also, separation, and more rarely shattering, were observed for head-on ( $X = 0$ ) collisions at the highest velocity (Fig. S7B). For the off-center separation, it was apparent that partial but incomplete mixing occurred. For the head-on shattering, it was not possible to quantify the extent of mixing in the microdroplet fragments, but it is unlikely that mixing was complete considering that fragmentation occurred nearly instantaneously but complete mixing takes  $\sim 200$   $\mu\text{s}$ .

It has been well established that the outcome of binary collisions (e.g., coalescence or fragmentation into smaller droplets) is related not only to the collision parameters such as  $D$ ,  $U$  and  $X$ , but to fluid properties, as well.<sup>17,18,23,24</sup> The nondimensional Weber number ( $We$ ), which scales the relative importance of fluid inertia to surface tension, is a parameter commonly used to relate collision parameters and fluid properties to collision outcomes, as given by Eq. S2

$$We = \frac{\rho D U^2}{\sigma} \quad (\text{S2})$$

where  $\rho$  and  $\sigma$  are the fluid density and surface tension, respectively.<sup>9,17,18,23,24</sup>  $We$  numbers are computed here using  $\rho$  and  $\sigma$  values of 1160  $\text{kg m}^{-3}$  and 73.9  $\text{mN m}^{-1}$ , respectively (values associated with 20%  $\text{H}_2\text{SO}_{4(\text{aq})}$ ). For our experiments, the transition between permanent coalescence and separation occurred between  $We \approx 27$  to 30, consistent with the predictions of Saroka and Ashgriz<sup>24</sup>. A size-dependence has been reported for this transition  $We$  value from coalescence to separation. For 10  $\mu\text{m}$  microdroplets, it is predicted that separation would begin to occur at  $We = 32.5$ ,<sup>24</sup> which is higher than for our 40  $\mu\text{m}$  microdroplets. For 75  $\mu\text{m}$  microdroplets, this value is predicted to be 22. For submicron droplets, this value may be as high as 40 before separation occurs, although we are unaware of a study that reports experimental observations of submicron collisions to confirm the  $We$  value of separation. Additional studies

are likely necessary to fully understand the extent of mixing in colliding microdroplets that do not permanently coalesce.

**Additional Discussion of Relating  $\tau$  to Microdroplet Fluid Dynamics.** While the initial trend in  $\tau$ , where  $\tau$  decreases with increasing  $U$ , is consistent with expectations of inertial mixing driven by convection, the reason for the subsequent increase in  $\tau$  for off-center collisions is not readily apparent. Previous studies have shown that internal flow patterns in colliding droplets are related to shape oscillations.<sup>23,24</sup> We thus hypothesize that variations in internal flow patterns due to differences in collision geometry are the source of the variation in  $\tau$  with  $X$ . To investigate this hypothesis further, we captured sequences of brightfield images of high-velocity collisions to qualitatively compare our observations with studies of internal microdroplet flow patterns reported elsewhere<sup>23,24</sup>.

As shown in Figure S6 for a high-velocity collision ( $U = 3.9 \pm 0.2$  m/s), the collision process evolves differently depending on the collision geometry. For a head-on collision (Fig. S6A), the droplet shape expands and contracts with an oscillation period of  $\sim 20$   $\mu$ s, coincident with the rapid underlying oscillations in  $I_x$  seen in Fig. 5B of the main text for  $X = 0$ ). This oscillation period is consistent with the linear oscillation frequencies of droplet coalescence.<sup>25</sup> Such shape oscillations have been shown to be effective at stimulating internal flows within colliding droplets.<sup>23</sup> These internal flows effectively transport fluid in multiple directions across the merged droplet diameter as the shape oscillates, as illustrated in Fig. S6A.

For the off-center collision shown in Fig. S6B, at the moment of collision, there is a relatively small portion of the original microdroplets that interact and form a liquid bridge, while the outer (non-interacting) portion of the microdroplets continues unimpeded in the original trajectory. Rather than a periodic shape oscillation, this causes the merged droplet to rotate about an axis perpendicular to the droplet trajectory (perpendicular to the image plane). Simulations of internal fluid flow in colliding off-center droplets have shown that the direction of fluid flow remains outward and is largely unidirectional.<sup>24</sup> This creates an inefficient mixing scenario where the initial inertia associated with the microdroplet collision does not readily stimulate internal fluid flow and circulation, as illustrated in Fig. S6B. Rather, much of the fluid from the original droplets remains compartmentalized at the ends of the droplet. The internal flows necessary for mixing likely do not manifest until contraction and relaxation of the stretched droplet. This suggests that for inertial mixing to be most effective, the collision must stimulate multidirectional internal flow. For high velocity off-center collisions, this is not the case, thus resulting in the large values of  $\tau$  relative to head-on collisions.

At lower velocities, once droplets come in to contact, surface tension dominates and merged microdroplets contract quickly and relax to a spherical shape on comparable timescales, regardless of  $X$ , as seen in Figure S8. Thus, at lower velocities, the rapid contraction of the liquid bridge and high internal pressures of small microdroplets appears sufficient to stimulate internal flow patterns that mix droplets on submillisecond timescales regardless of  $X$ .

**Generalizations of Mixing Dynamics.** Although we speculate that differences in internal flow patterns are the driving force for the variation in  $\tau$  with  $X$ , a quantitative description (e.g., a simulation) of how these internal flows influence mixing dynamics is beyond the scope of this article. However, to facilitate the applicability of merged-droplet on-demand techniques in chemical analysis, we qualitatively constrain the conditions where collision geometry appears most important on mixing dynamics.

It has been well established that the outcome of binary collisions (e.g., coalescence or fragmentation into smaller droplets) is related not only to the collision parameters such as  $D$ ,  $U$  and  $X$ , but to fluid properties, as well.<sup>17,18,23,24</sup> We number, which scales the relative importance of fluid inertia to surface tension, is a parameter commonly used to relate collision parameters

and fluid properties to collision outcomes, as given by Eq. S2. It follows that through its dependence on  $U$ ,  $We$  may provide similar insight into trends in  $\tau$ .

A plot of  $\tau$  as a function of  $We$  is shown in Figure S9, which exhibits the same trends as those in Fig. 6 of the main text, with regions of distinct mixing dynamics observed, which depend on the value of  $We$ . These regions and trends are shown in Fig. S9.

From a close analysis of the behavior of  $\tau$  over the full range of  $We$ , it is possible to make generalized recommendations for experimental conditions for microdroplet mixing. Fig. S9 suggests that maintaining a  $We \approx 0.01$  to 1 (region I) ensures repeatable mixing times and sub-millisecond mixing times ( $\sim 500$  to  $900 \mu\text{s}$ ) for the droplet sizes used here. For applications where a kinetic measurement is made within milliseconds of droplet mixing, this reliability and repeatability would be beneficial. Faster mixing times can be achieved at higher  $We$  (region II; e.g.,  $\tau \approx 200 \mu\text{s}$  at  $We \approx 25$ ), although  $\tau$  deviates by a factor of 5 to 6 depending on  $X$ . Thus, at high  $We$ , it may be necessary to have knowledge of and fine control over  $X$ . At the highest  $We$  values (region III) droplets separate or fragment (Fig. S7). Thus, it appears prudent to maintain a  $We < 30$ , i.e., below the separation/fragmentation threshold (which is expected to be different for different droplet diameters)<sup>24</sup>, if complete mixing is necessary.

**Sample Volume Consumption Rate.** The sample volume consumption rate for the colliding-droplet microreactor is low and can be tailored to a specific application as a result of being on-demand (i.e., no sample is forced through the droplet dispensers). The volume of a  $40 \mu\text{m}$  microdroplet is  $\sim 35 \text{ pL}$ . Thus, because droplets are generated on-demand, a single experiment of merging microdroplets could use as little as  $\sim 70 \text{ pL}$ . In the experiments reported here, droplets were dispensed at a repetition rate of  $2 \text{ kHz}$  (i.e.,  $2000 \text{ droplets/s}$ ). Thus, the volume consumption rate for these experiments was  $\sim 140 \text{ nL/s}$ . Consumption rate would be even lower at lower droplet generation rates.